Evolution of Dipolar Boson Stars and Head-on Collisions of Spherical Boson Stars

Pedro Ildefonso
pedro.ildefonso@tecnico.ulisboa.pt

Instituto Superior Técnico, Lisboa, Portugal

November 2021

Abstract

We probe the hypothesis of forming static (in the spacetime metric) dipolar like configurations of boson stars (BSs) from the head-on collision of two ground state BSs with opposite phases. We perform non-linear numerical simulations of ground state BSs in a model without self-interactions (mini-BSs) and show that the instabilities created during the collision lead to the gravitational collapse to a black hole (BH); however, by introducing fourth and sixth order self-interacting terms in the scalar potential (Q-stars), we show that the binary is robust enough to withstand at least 16 repetitive collisions. These results support the healing power of self-interactions and provide a candidate mechanism for the formation of dipolar BSs. With this in mind, we study the dynamical stability of dipolar BSs in the model of Q-stars (doublet Q-stars). We show the existence of two (candidate) stable branches: the relativistic stable branch (for scalar field frequencies near the lower limit) and the Newtonian stable branch (for scalar field frequencies near the maximum value). Solutions outside of these branches show a migrating behaviour, whose final destiny still requires further investigation.
Keywords: Scalar field, Klein-Gordon, general relativity, binary, dipolar

1. Introduction

Scalar classical fields, more specifically complex scalar fields, feature, in the Klein Gordon (KG) theory minimally coupled to Einstein's gravity, macroscopic stable configurations named Boson Stars (BSs) [1]. In recent illustrations, dynamically robust Boson Stars (BSs) were considered good candidates to match the predictions made for the merger of two BHs [2] and to mimic the (effective) shadow of a black hole shadow [3]. Their role as BHs mimickers in other models [4], and their feature as good candidates for some of the DM sources in our universe [5], supports their astrophysical interest. Moreover, the advances in modern astronomy, e.g. the increasing precision of gravitational wave detectors [6], places us on the verge of discovering new and more accurate results capable of distinguishing the nature and behaviour of these compact objects.

In this sense, establishing the models that comprise the different families of BSs is essential to build a collection of dynamically stable BSs as the theoretical basis for the analysis of experimental data. One such family is that of dipolar BSs, a particular case of the large class of multipolar BSs introduced by Herdeiro et al. [7]. In this work, we shed some light on the unstudied dynamics of these solutions while establishing a connection between their formation mechanism and the final state of a head-on collision between two spherical BSs. Additionally, We argue that head-on collisions between two ground state (spherical) BSs can only produce a stable binary system if the model contains self-interactions.

We give, in section 2, a general background knowledge on ground state BSs with and without self-interactions and on excited BSs, with the particular case of a dipolar BSs. We display our results in section 5, where we show that the head-on collision between two ground state stable BSs without self-interactions (mini-BSs) leads to an unstable binary system. Then, in section 6, we perform the same study but for BSs with self-interactions (Q-stars), where by following and extending the study of [8], we show robust stability for the case of head-on binaries in phase opposition. Ultimately, we study in section 7 the dynamical robustness of dipolar BSs with a self-interacting scalar potential, named "doublet Q-stars".

2. Background

The action S for Einstein's gravity minimally coupled to a complex massive scalar field ϕ reads,

$$S = \int d^4x\sqrt{-g}\left[\underbrace{\frac{R}{16\pi}}_{\mathcal{L}_g} - \underbrace{\frac{1}{2}g^{ab}\left(\partial_a\phi^*\partial_b\phi + \partial_b\phi^*\partial_a\phi\right) - U\left(|\phi|^2\right)}_{\mathcal{L}_\phi}\right], \quad (1)$$

where $\mathcal{L}_g$ and $\mathcal{L}_\phi$ are the Einstein-Hilbert and the scalar field terms of the Lagrangian. The above equation leads

to the EFEs and the KG equation,

$$R_{ab} - \frac{1}{2} g_{ab} R = 8\pi T_{ab}, \tag{2}$$

$$\nabla^a \nabla_a \phi = \frac{\partial U}{\partial |\phi|^2} \phi, \tag{3}$$

respectively, where the stress-energy tensor reads,

$$\begin{aligned} T_{ab} =& \nabla_a \phi^* \nabla_b \phi + \nabla_b \phi^* \nabla_a \phi \\ & - g_{ab} \left[\nabla_c \phi^* \nabla^c \phi + U \left(|\phi|^2 \right) \right]. \end{aligned} \tag{4}$$

Together, equations (2) and (3) compose the Einstein-Klein-Gordon (EKG) system of equations. Finding a solution for this system implies finding a suitable function ϕ for a given scalar potential U. For BSs the simplest ansatz for scalar field is the harmonic one,

$$\phi = \phi_0 \left(r, \theta, \varphi \right) e^{-i\omega t}, \tag{5}$$

where ω is the oscillation frequency of the star and $\phi_0 \left(r, \theta, \varphi \right)$ is a real spatial profile function.

Ground state BSs, that lie within the spherical sector, i.e. have a spherically symmetric scalar field density distribution,

$$\phi \left(r, t \right) = \phi_0 \left(r \right) \ e^{-i\omega t}, \tag{6}$$

where $\phi_0 \left(r \right) \sim e^{-r\sqrt{\mu^2 - \omega^2}} / r$. In particular, those obeying a free-field potential,

$$U \left(|\phi|^2 \right) = \mu^2 \ |\phi|^2, \tag{7}$$

are labelled "mini-BSs". These possess a well-founded formation mechanism [9] while fulfilling the criteria of dynamical stability [10, 11]. Additionally, preliminary tests on binary systems have showed dynamical robustness under head-on and orbital collisions [12, 13]. Similarly, BSs whose scalar field obeys a sextic self-interacting scalar potential,

$$\begin{aligned} U \left(|\phi|^2 \right) &= \mu^2 \ |\phi|^2 \ \left[1 - 2 V_\lambda \ |\phi|^2 \right]^2 \\ &= \mu^2 \ \phi_0^2 \ - \ 4 \ \mu^2 \ V_\lambda \ \phi_0^4 \ + \ 4 \ \mu^2 \ V_\lambda^2 \ \phi_0^6, \end{aligned} \tag{8}$$

denoted as "Q-stars", where $V_\lambda = {}^1\!/_{\sigma_0^2}$ ($\sigma_0 > 0$ is a constant that determines the compactness of the star), also possess a well-founded formation [14] and stability [15, 16] mechanisms, and have proved, as well, to be dynamically robust in binary systems [8].

BSs in excited states, also denoted as the non-spherical sector of multipolar BSs, correspond to the non-zero (ℓ, m) sector of the akin quantum numbers of the hydrogen orbitals [17]. We focus our attention on the ($n = 2$, $\ell = 1$, $m = 0$) case, also denoted as a dipolar BS. Introduced by Herdeiro et al. [7] as solutions obeying a free-field potential, they represent axially symmetric configurations of the scalar field,

$$\phi \left(r, \theta, t \right) = \phi_0 \left(r, \theta \right) \ e^{-i\omega t}, \tag{9}$$

with an odd-parity distribution that resembles the configuration of the final state of head-on binary of spherical BSs, i.e. in the ground state, with their scalar field oscillating with opposite phases. For the particular case of self-interacting dipolar BSs, i.e. obeying a scalar potential of a Q-star, named "doublet Q-stars" [18], so far, no model have been constructed, leaving their stability spectrum an open question.

3. Numerical framework

The code employed for the numerical simulations makes use of the EinsteinToolkit (ET) [19, 20] infrastructure. The latter is an open source, community-driven infrastructure for numerical relativity that uses the BSSN (Baumgarte, Shapiro, Shibata, Nakamura) evolution system [21, 22] with standard "moving puncture" Gamma-driver and 1 + log gauge conditions [23]. Divided into different "thorns", the toolkit provides the tools to numerically evolve the EKG equations with the Cactus Computational Toolkit [24, 25, 26].

In the 3+1 formalism, to characterize our spacetime we define the line element as,

$$ds^2 = -\alpha^2 dt^2 \ + \ \gamma_{ij} \left(dx^i \ + \ \beta^i dt \right) \left(dx^j \ + \ \beta^j dt \right), \tag{10}$$

where α is the lapse function, β^i is the shift vector, and γ_{ij} is the induced metric in each spatial foliation. Together with the line element, the extrinsic curvature is given as,

$$K_{ij} = \ -\frac{1}{2\alpha} \left(\frac{\partial}{\partial t} - \mathscr{L}_{\boldsymbol{\beta}} \right) \gamma_{ij}, \tag{11}$$

and, analogously, the "canonical momentum" of the complex scalar field ϕ is,

$$K_\phi = \ -\frac{1}{2\alpha} \left(\frac{\partial}{\partial t} - \mathscr{L}_{\boldsymbol{\beta}} \right) \phi, \tag{12}$$

where $\mathscr{L}$ is the Lie derivative. The full EKG system equations reads,

$$\partial_t \gamma_{ij} = -\ 2\alpha K_{ij} + \mathcal{L}_\beta \gamma_{ij}, \tag{13}$$

$$\begin{aligned} \partial_t K_{ij} =& -\ D_i \partial_j \alpha + \alpha \left(R_{ij} - 2 K_{ik} K^k_j + K K_{ij} \right) \\ & + \mathcal{L}_\beta K_{ij} + 4\pi\alpha \left[\left(S - \rho \right) \gamma_{ij} - 2 S_{ij} \right], \end{aligned} \tag{14}$$

$$\partial_t \phi = -\ 2\alpha K_\phi + \mathcal{L}_\beta \phi, \tag{15}$$

$$\begin{aligned} \partial_t K_\phi =& \alpha \left(K K_\phi - \frac{1}{2} \gamma^{ij} D_i \partial_j \phi + \frac{1}{2} \Box \phi \right) \\ & - \frac{1}{2} \gamma^{ij} \partial_i \alpha \partial_j \phi + \mathcal{L}_\beta K_\phi. \end{aligned} \tag{16}$$

where D_i denotes the covariant derivative with respect to the 3-metric, and the source terms are given by,

$$\rho \equiv T_{ab} n^a n^b, \tag{17}$$

$$\mathrm{J}_i \equiv -\ \gamma^a_i T_{ab} n^b, \tag{18}$$

$$S_{ij} \equiv \gamma^a{}_i \gamma^b{}_j T_{ab}, \tag{19}$$

$$S \equiv \gamma^{ij} S_{ij}, \tag{20}$$

where ρ, S_i, S_{ij} and S denote the energy density, momentum density, stress, and the trace of the stress as observed by a normal observer (moving along the normal vector n^a), respectively.

For numerical evolutions, it is convenient to rewrite the equations above in the strongly hyperbolic BSSN scheme. In this scheme we introduce a conformal metric $\tilde{\gamma}_{ij}$,

$$\gamma_{ij} = \frac{1}{\chi}\tilde{\gamma}_{ij}, \tag{21}$$

related to γ_{ij} by a conformal factor $\chi = (\det\gamma_{ij})^{-1/3}$ chosen such that $\det\tilde{\gamma}_{ij} = 1$ holds at all times. Next, we split the extrinsic curvature into a trace part (K) and a traceless conformal part $\left(\tilde{A}_{ij}\right)$,

$$\tilde{A}_{ij} = \chi\left(K_{ij} + \frac{1}{3}K\gamma_{ij}\right), \tag{22}$$

where the traceless conformal part is decomposed as: $\tilde{A}_{ij} = \chi A_{ij}$. The full EKG system reads,

$$\begin{aligned}
\partial_t\tilde{\gamma}_{ij} &= \beta^k\partial_k\tilde{\gamma}_{ij} + 2\tilde{\gamma}_{k(i}\partial_{j)}\beta^k \\
&\quad - \frac{2}{3}\tilde{\gamma}_{ij}\partial_k\beta^k - 2\alpha\tilde{A}_{ij}, && (23)\\
\partial_t\chi &= \beta^k\partial_k\chi + \frac{2}{3}\chi\left(\alpha K - \partial_k\beta^k\right), && (24)\\
\partial_t\tilde{A}_{ij} &= \beta^k\partial_k\tilde{A}_{ij} + 2\tilde{A}_{k(i}\partial_{j)}\beta^k - \frac{2}{3}\tilde{A}_{ij}\partial_k\beta^k \\
&\quad + \chi\left(\alpha R_{ij} - D_iD_j\alpha\right)^{\mathrm{TF}} \\
&\quad + \alpha\left(K\tilde{A}_{ij} - 2\tilde{A}^k_i\tilde{A}_{kj}\right) \\
&\quad - 8\pi\alpha\left(\chi S_{ij} - \frac{S}{3}\tilde{\gamma}_{ij}\right), && (25)\\
\partial_t K &= \beta^k\partial_k K - D^kD_k\alpha + \alpha\left(\tilde{A}^{ij}\tilde{A}_{ij} + \frac{1}{3}K^2\right) \\
&\quad + 4\pi\alpha\left(\rho + S\right), && (26)\\
\partial_t\tilde{\Gamma}^i &= \beta^k\partial_k\tilde{\Gamma}^i - \tilde{\Gamma}^k\partial_k\beta^i + \frac{2}{3}\tilde{\Gamma}^i\partial_k\beta^k \\
&\quad + 2\alpha\tilde{\Gamma}^i_{jk}\tilde{A}^{jk} + \frac{1}{3}\tilde{\gamma}^{ij}\partial_j\partial_k\beta^k \\
&\quad + \tilde{\gamma}^{jk}\partial_j\partial_k\beta^i - \frac{4}{3}\alpha\tilde{\gamma}^{ij}\partial_j K \\
&\quad - \tilde{A}^{ij}\left(3\alpha\chi^{-1}\partial_j\chi + 2\partial_j\alpha\right) - 16\pi\alpha\chi^{-1}j^i, && (27)\\
\partial_t\phi &= -2\alpha K_\phi + \mathcal{L}_\beta\phi, && (28)\\
\partial_t K_\phi &= \alpha\left(KK_\phi - \frac{1}{2}\gamma^{ij}D_iD_j\phi + \frac{1}{2}\Box\phi\right) \\
&\quad - \frac{1}{2}\gamma^{ij}\partial_i\alpha\partial_j\phi + \mathcal{L}_\beta K_\phi. && (29)
\end{aligned}$$

Additionally, our system is subject to a set of constraints given by the Hamiltonian and Momentum constraints,

$$\mathcal{H} \equiv R + K^2 - K_{ij}K^{ij} = 16\pi\rho, \tag{30}$$

$$\mathcal{M}_i \equiv D_iK - D^jK_{ij} = -8\pi j_i, \tag{31}$$

respectively.

4. The ansatz

4.1. Spherical boson stars

We consider, for isotropic coordinates, a spherically symmetric scalar field of the form (6), with $\omega > 0$, and a spherically symmetric metric of the form,

$$\begin{aligned}
ds^2 = -e^{2F_0(r)}dt^2 &+ e^{2F_1(r)}\left(dr^2 + r^2d\theta^2\right. \\
&\left. + r^2\sin^2\theta d\varphi^2\right),
\end{aligned} \tag{32}$$

where F_0 and F_1 are the metric functions. We impose the following set of boundary conditions:

$$\partial_rF_{0,1}|_{r=0} = 0, \quad \partial_r\phi_0|_{r=0} = 0, \tag{33}$$

$$F_{0,1}|_{r=\infty} = \phi_0|_{r=\infty} = 0, \tag{34}$$

The solutions are constructed by employing the same approach as for Kerr BHs with scalar hair, see e.g. the description in [27].

4.2. Head-on boson star binary

For a system of two spherically symmetric BSs, placed along the $x-$axis at positions $r_1 : (x_1,\ 0,\ 0)$ and $r_2 : (x_2,\ 0,\ 0)$, whose purpose is to collide head-on, with no boost, we define the system's initial data with: 1) a spacetime metric, g_{ab}, which is the sum of each solution's metric, $g^{(i)}_{ab}$ ($i = 1,\ 2$), minus the flat metric η_{ab}; and 2) a complex scalar field, ϕ, as the sum of each star's scalar field, $\phi^{(i)}$,

$$g_{ab} = g^{(1)}_{ab} + g^{(2)}_{ab} - \eta_{ab}, \tag{35}$$

$$\phi\left(t,r\right) = \phi^{(1)}_0\left(r_1\right)e^{-i\omega t} + \phi^{(2)}_0\left(r_2\right)e^{-i(\omega t+\vartheta)}, \tag{36}$$

where one of the solutions possesses a phase difference of ϑ relative to the other, to allow modelling systems that can have identical or non-identical stars. However, given the non-linearity of the EKG equations, the superposition between two solutions is not a solution of these equations. By super-positioning the two solutions, we incur in a violation of the EKG equations, which can be quantified with the Hamiltonian constraint equation (30). We will see that by increasing the distance between the stars, that is, by increasing $D \equiv |x_1 - x_2|$, the Hamiltonian constraint violation decays exponentially. As such, by placing the stars sufficiently apart from each other, we can minimise the violation and be confident that the results of our simulations have relevant physical meaning.

Regarding the phase difference ϑ between the two stars, we will see that the binary will behave differently for different values between $0 \leq \vartheta \leq \pi$. More specifically, we will cover two different scenarios for two different values of ϑ, $\vartheta = \{0, \pi\}$: the first, where both stars are identical, i.e. are in-phase ($\vartheta = 0$), we denote by *ip-BBS* scenario; the other, where they are in phase opposition, $\vartheta = \pi$, we denote by *op-BBS* scenario. For the latter scenario the anti-symmetric property of the scalar field ϕ on the anti-symmetry plane (corresponding to the $y = 0$ plane if the collision is being made along the $x-$axis) causes an effect similar to a repulsive force that acts and overcomes gravity at short distances, preventing the merger from happening [28].

4.3. Dipolar boson stars

Dipolar BSs are given their name due to a dipolar distribution of their scalar field. Their scalar field function has

the form of an axisymmetric harmonic ansatz (5) and the scalar field amplitude, ϕ_0, is given as,

$$\phi_0 \equiv \sum_{\ell,\ m} R_\ell\,(r)\ \ Y_{\ell m}\,(\theta,\varphi)\,, \tag{37}$$

where R_ℓ and $Y_{\ell m}$ are the radial amplitude, and the spherical harmonics, for $n=2,\ \ell=1,\ m=0$. For the spacetime metric we assume an axisymmetric ansatz as well,

$$\begin{aligned} ds^2 = -e^{2F_0(r,\ \theta)}dt^2 \ &+\ e^{2F_1(r,\ \theta)}\left(dr^2\ +\ r^2 d\theta^2\right) \\ &+\ e^{2F_2(r,\ \theta)}r^2\sin^2\theta\ d\varphi^2, \end{aligned} \tag{38}$$

in terms of the three functions $F_{0,\ 1,\ 2}$, with which we provide the system's initial data, along with the scalar field amplitude, ϕ_0. Their energy and Noether charge densities are localised in two distinct components, named poles, located symmetrically in the $z-$axis at $z=\pm z_0$, where the proper distance between these components is defined as,

$$L = 2\int_0^{z_0} dr\ e^{F_1(r,0)}. \tag{39}$$

Our initial data is subject to the following set of boundary conditions:

$$\partial_r F_{0,1,2}|_{r=o} = \partial_r\phi_0|_{r=0} = 0, \tag{40}$$

$$F_{0,1,2}|_{r=\infty} = \phi_0|_{r=\infty} = 0, \tag{41}$$

$$\partial_\theta F_{0,1,2}|_{\theta=0,\pi} = \partial_\theta\phi_0|_{\theta=0,\pi} = 0. \tag{42}$$

Also the metric functions are invariant *w.r.t.* a reflection in the equatorial plane, $\theta=\pi/2$, while the scalar field changes sign, which implies,

$$\partial_\theta F_{0,1,2}|_{\theta=\pi/2} = \phi_0|_{\theta=\pi/2} = 0. \tag{43}$$

5. Dynamical systems of mini-BSs

Throughout the following sections, we will be working in adimensional units. The time t and length r variables, previously given in geometrical units ($[t]=[r]=L$), are now multiplied by the reduced mass μ, which has units of L^{-1}. Time and length are therefore given in these dimensionless units, as $[t\mu]=[r\mu]=1$.

The first family of BSs, named mini-BSs, are static (in the spacetime metric), spherically symmetric configurations whose scalar field obeys the free-field potential (7).

We follow the geometrical unit convention,

$$c\ =\ G\ =\ 1, \tag{44}$$

with,

$$\mu\ =\ 1.$$

We analyse the five solutions, and their binaries, highlighted in Figure 1 and presented with numbers 1 to 5 in Table 1. Since BSs have no defined surface, given their matter density exponential fall-off, we define the radius R_{99} as the perimetral radius R[1], derived from the radial coordinate r as $R_{99}=e^{F_1}r$, containing 99% of the BS mass. We pay particular interest to these five solutions given their region in the ADM mass/Noether charge *vs.* scalar field frequency diagram in Figure 1. Here we look at the difference between the Noether charge and the ADM mass, i.e. the system's binding energy $E=M-Q\mu$, in units with $\mu=1$, to provide a preliminary criterion for stability: in the case where $E>0$, that is, when the system possesses an excess of energy in the form of binding energy, the star becomes unstable against fission of its bosonic particles into unbound particles [29]. In the diagram, this occurs for scalar field frequencies $\omega/\mu\sim[0.77,\ 0.86]$ and ADM masses/Noether Charges between $[0.2,\ 0.5]$; if the system has no excess of energy, which is the case for our five solutions, we expect the solutions to be stable. However, to firmly establish their stable nature, we need further stability analysis, e.g. linear perturbation theory or, in our case, numerical simulations.

[1] radial coordinate R that defines a circumference along the equatorial plane with perimeter $\simeq 2\pi R$

Table 1: Mini boson star models.

Solutions	ω/μ	$\phi_0\,(r=0)$	$\mu M_{\mathbf{ADM}}$	μR_{99}
1	0.85	0.056	0.633	7.270
2	0.88	0.042	0.624	8.855
3	0.89	0.037	0.616	9.493
4	0.90	0.033	0.605	10.213
5	0.95	0.015	0.490	16.207

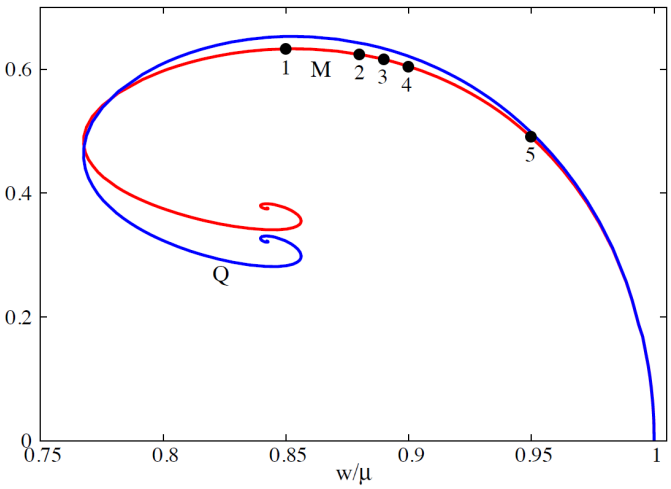

Figure 1: The domain of existence of mini-BSs in an ADM mass (M)/Noether charge (Q) *vs.* complex scalar field frequency (ω/μ) diagram. The highlighted points represent the five solutions analysed in this section.

All binaries, in both the ip-BBS and op-BBS scenarios, showed the same final fate—the gravitational collapse to a BH. In the op-BBS a scalar field repulsion was observed for the 4th and 5th solutions shortly before the gravitational collapse under the strong instabilities. Therefore, we can argue that such solutions, under such extreme perturbations, are not dynamically robust, even though being dynamically stable when isolated.

6. Dynamical systems of Q-stars

We question whether a theory with self-interactions produces the mechanism to allow the dynamical robustness

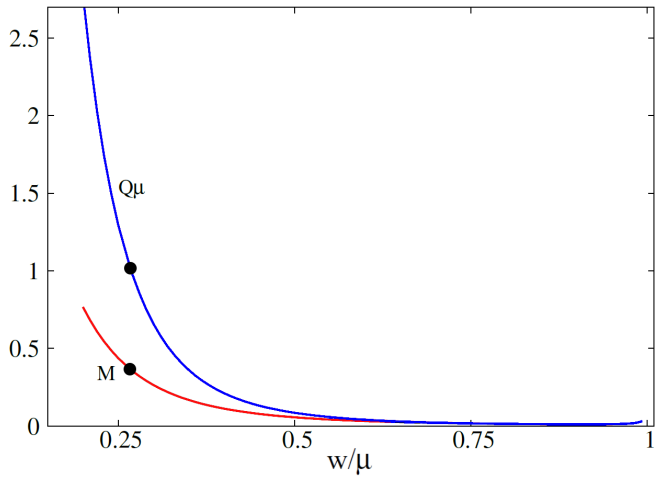

Figure 2: The (preliminary) domain of existence of Q-stars in an ADM mass (M)/Noether charge (Q) *vs.* complex scalar field frequency (ω/μ) diagram. The highlighted point represents the solution analysed in this Chapter.

Table 2: Q-star models.

Solutions	ω/μ	$\phi_0\,(r=0)$	$\mu M_{\mathbf{ADM}}$	μR_{99}
1	0.27	0.036	1.456	8.898

of its solutions in a head-on collision. In this sense, we introduce the second family of BSs, named Q-stars, whose scalar field obeys the attractive scalar potential (8).

We follow the geometrical unit system (44) with,

$$\mu\sigma_0\sqrt{8\pi} \;=\; 1,$$

where,

$$\sigma_0 = 0.05.$$

Following the line of work of [8], we construct the solution depicted in Figure 2 and defined in Table 2 by its amplitude, mass and radius.

We evolve both the single and the binary configurations in a grid with five and four refinement levels, respectively. We change the grid's size and resolutions to $X \in [-255, +255]$ and $Y, Z \in [0, +255]$ (in adimensional units), $\Delta X^i = 0.25$, in the innermost level, and the time resolution to: $\Delta t = 0.1\Delta X^i = 0.025$.

6.1. Single systems

The solution was evolved under no external perturbations (other than numerical noise) up to $t\mu = 140$ and showed no formation of instabilities. In Figure 3, the real component of ϕ, extracted from the numerical evolution at $r_{\rm ext} = 8.104$, is plotted against its analytical counterpart, showing agreement between both.

6.2. Binary systems

For the binary scenario we placed both stars along the $x-$axis at a distance of $D\mu = 80$, that is, at $x_1 = -40$ and $x_2 = 40$.

We begin by evolving the binary within the ip-BBS scenario, i.e. with identical stars, as depicted in Figure 4,

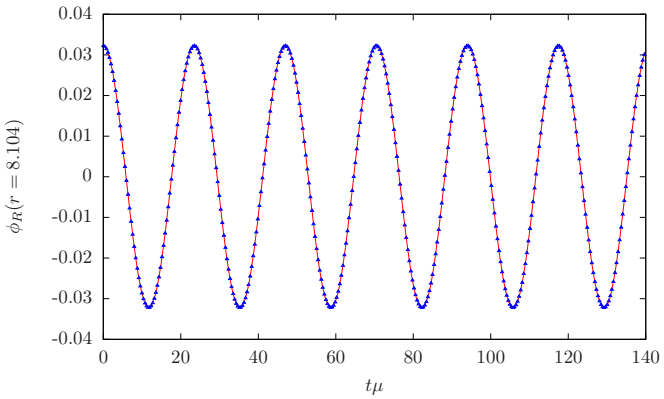

Figure 3: *Single Q-star with* $\omega/\mu = 0.27$. Evolution of the real part of ϕ at $r\mu = r_{\rm ex} = 8.104$. The analytical expected value — $0.0328\cos(0.27t)$ — is illustrated as the red line while the numerical evolution is shown by the blue triangles.

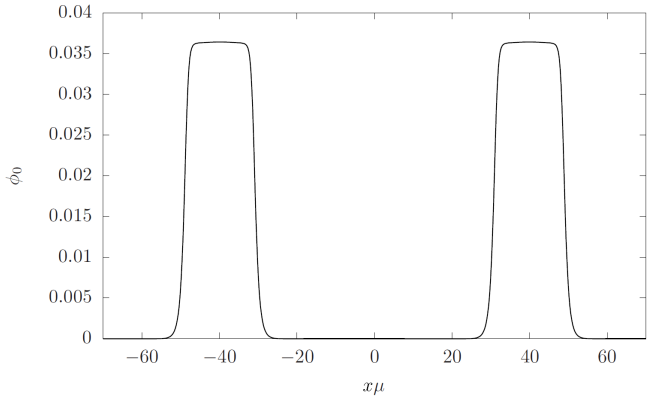

Figure 4: *Head-on collisions of Q-stars in the ip-BBS scenario.* Real part of the scalar field for the Q-star binary in the ip-BBS scenario. The binary has its stars centered at $x\mu = \{-40, 40\}$.

up to $t\mu = 800$. Upon merger the binary forms a single highly perturbed star. The resulting star oscillates violently around the origin, radiating the excess of kinetic energy via gravitational wave radiation and by ejecting part of its scalar field as a method of gravitational cooling, matching the results in [8]. The snapshots of the scalar field in the plane $z = 0$ are shown in Figure 5 (top panel), revealing the behaviour described above.

Given our motivation in finding stable configurations of binaries, we focus our attention on the op-BBS scenario. We evolve two stars with opposite phases in the scalar field internal oscillation, as Figure 6 shows, up to $t\mu \sim 6500$. Our results show that, as the stars come together, a repulsive interaction between the two emerges, causing them to bounce off each other and return to almost 85% of their initial position, reaching a distance of $r\mu \sim 34$ after the first bounce. As the stars reach this distance, as we shall refer to as "rebound distance", they begin their second approach with an identical behaviour as in the first approach, and a second bounce occurs, as Figure 5 shows.

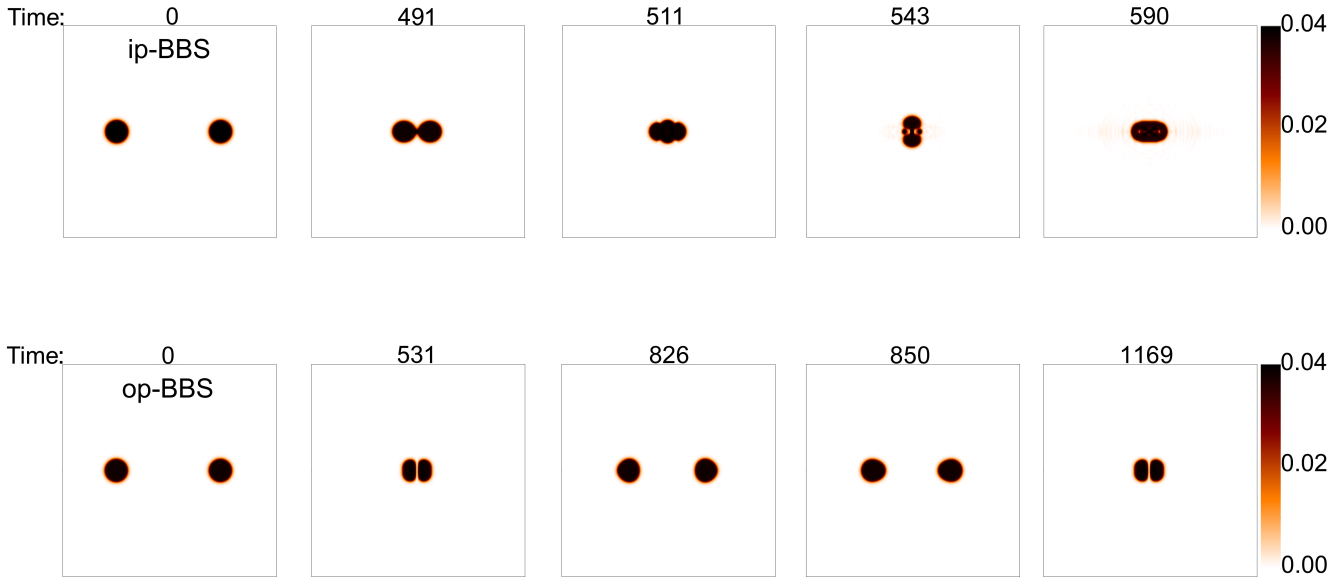

Figure 5: *Head-on collisions of Q-stars.* Time snapshots of the scalar field density in the plane $y = 0$ where, in the first row, the binary is in-phase and, in the second row, in phase opposition. **ip-BBS:** the initial conditions, at $t = 0$; the moment when the stars first touch; the merger; the last two snapshots show the violent oscillations of the resulting star while radiating part of its scalar field as the effect of gravitational cooling. **op-BBS:** the initial conditions; the first bounce due to the presence of a strong repulsive force that acts at short distances; the rebound of both stars; the presence of internal oscillations that change the shape of the star; the second bounce. Link to movies [30, 31].

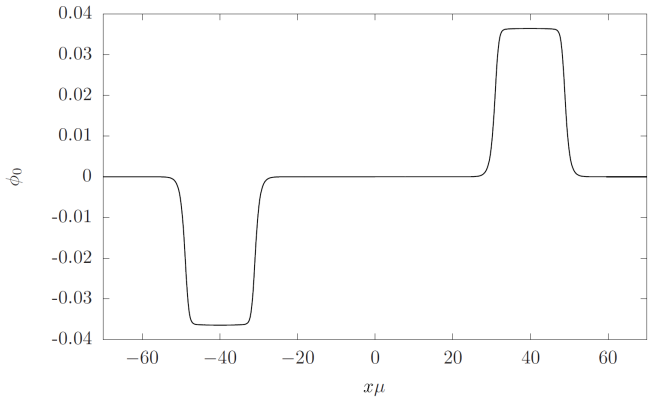

Figure 6: *Head-on collisions of Q-stars in the op-BBS scenario.* Real part of the scalar field at $t = 0$ for the Q-star binary in the op-BBS scenario. The binary has its stars centered at $x\mu = \{-40, 40\}$.

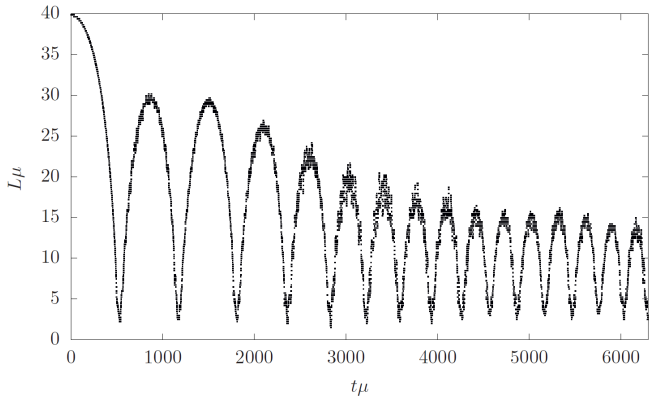

Figure 7: *Head-on collisions of Q-stars in the op-BBS scenario.* The motion, along the $x-$axis, of one of the stars is shown here as a function of time.

This behaviour continues throughout the full simulation time, with each collision being less energetic than the previous, manifested by a decrease in the rebound distance, as Figure 7 shows. We have obtained 16 bounces for a simulation time of about $t\mu \sim 6500$. Each bounce occurs at $t\mu \sim \{500,\ 1200,\ 1800,\ 2400,\ 2900,\ 3300,\ 3700,\ 4000,\ 4300,\ 4600,\ 4900,\ 5200,\ 5500,\ 5800,\ 6000,\ 6300\}$. At each collision, the system loses kinetic energy in two ways: via gravitational radiation, as is shown in Figure 8; and by converting it to internal vibration modes of each star [2].

7. Dynamical doublet Q-stars

We now evaluate the dynamical properties dipolar BS solutions, obeying the self-interacting scalar potential (8), named doublet Q-stars [18]. We impose the same convention for the unit system as in section 6. We construct eight different solutions, depicted in Figure 9 and Table 3, for different values of the rescaled frequency, ω/μ, the scalar field amplitude at the center of one of the poles ($r = r_c$), $\phi_0\,(r = r_c)$, the rescaled mass ADM, $\mu M_{\rm ADM}$, and the rescaled proper distance between the two poles (of each dipole), μL. We evolve these numerically, in a

[2]The vibration modes of each star can be clearly seen in the simulation animation [31].

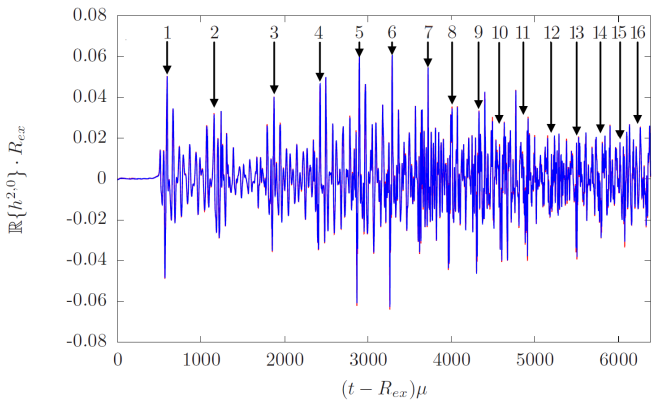

Figure 8: *Head-on collisions of Q-stars in the op-BBS scenario.* The real part of the $l = 2$, $m = 0$ mode of the Ψ_4 describing the gravitational wave emission of the binary extracted at $R_{\rm ex}\ \mu = 160$ (red line) and $R_{\rm ex}\ \mu = 200$ (blue line), as a function of time. The different instances at which the bounces takes place are numbered with black arrows.

Table 3: Doublet Q-stars models.

Sol. #	ω/μ	ϕ_0 $(r = r_c)$	$\mu M_{\rm ADM}$	$\mu^2 Q$	μL
1	0.25	0.036	2.799	7.996	8.795
2	0.27	0.037	2.333	6.226	8.550
3	0.85	0.032	0.099	0.097	6.449
4	0.89	0.029	0.094	0.090	7.108
5	0.94	0.022	0.097	0.094	8.767
6	0.98	0.010	0.153	0.152	13.741
7	0.99	0.004	0.223	0.221	20.731
8	0.997	0.001	0.185	0.185	42.463

grid with three refinement levels. The grid has a rectangular shape on the two innermost levels and an overall size of $X, Y \in [0,\ +128]$ and $Z \in [-128,\ +128]$ (in adimensional units). We impose symmetry on the x and $y-$axis given that the solution is axisymmetric and its dipoles are placed along the $z-$axis. For all but the solution number 8, the innermost level has a resolution of $\Delta X^i = 0.25$ and we use a evolution time step of $\Delta t = 0.025$. For the last solution, given its large radius and our numerical time limitations, we decrease the innermost level and time resolutions to $\Delta X^i = 0.5$ and $\Delta t = 0.05$, respectively.

The scalar field profiles (along the $z-$axis) at $t = 0$ are shown, for the eight solutions, in Figure 10. We observe, from Figure 9, that doublet Q-stars have solutions with frequencies ranging from $\omega_{\rm min}/\mu \sim 0.152$ to the general upper limit of BSs, $\omega_{\rm max}/\mu = 1$. Within our eight solutions, those with smaller frequencies, $\omega/\mu = \{0.25,\ 0.27\}$, present shapes for each pole, similar to the Q-star solution studied in section 6, i.e. highly compact and localised distributions of the scalar field. However, as we increase the scalar field frequency, the solution becomes less compact and more dispersed across space.

Regarding the scalar field oscillation of each solution we show complete agreement between the numerical and the analytical data for all solutions. In Figure 11 we show as an example the scalar field oscillation of 1st solution.

All solutions, with exception on the last, were evolved up to a minimum of $t\mu = 3000$. Those that presented growing instabilities within the first $\Delta t\mu = 3000$ were evolved to longer simulation times to infer the nature of the instabilities. Examples of these are the 4th, 5th, 6th and 7th solutions. Overall, these four solutions show three different unstable behaviours, with the middle 5th and 6th showing similar behaviours, depicted in Figure 12.

The *4th solution*, which took the longest to become highly unstable, shows the dispersion of scalar matter on one of its poles, disturbing the second pole and, consequently, also dispersing all its scalar matter to infinity. The *5th* and *6th solutions*, at early times, decay to a more stable and compact configuration, ejecting part of its scalar field to infinity. The scalar field repulsion, between the poles, ceases to be able to hold the gravitational pull and the poles attract each other, behaving similarly to a head-on binary in the op-BBS scenario; the poles then collide inelastically, eventually reaching the rebound distance, which is roughly $r\mu \sim 8.3$ and $r\mu \sim 13.2$, and attract each other again performing a second inelastic collision. The process is repeated, for each solution, until the end of the simulation, with the 5th and 6th solutions performing in total 18 and 11 collisions, respectively. Finally, the *7th solution*, given its growing size and decreasing density, shows a growing expansion of its scalar field distribution, reaching a maximum size at $t\mu \sim 5000$.

This behaviour seems to indicate the migration of, at least, the 5th, 6th and 7th solutions to other solutions within the stable branch. One way to conclude which solutions these migrate to is by analysing the evolution of the scalar field frequency, ω/μ, the ADM mass, $M_{\rm ADM}\mu$, and the distance $L\mu$ between the centre of one pole and the origin. The preliminary migration directions are depicted in Figure 13.

8. Conclusions

The unstable behaviour of mini-BSs binaries shows that they do not possess the mechanism to allow them to remain dynamically robust throughout a collision with a companion BS, clarifying the work of Palenzuela et al. [12] on the dynamical stability of such compact objects.

On the other hand, Q-star binaries, containing self-interactions, remained dynamically robust for an extended period of simulation time, equivalent to sixteen repetitive collisions, with each collision, causing the binary to lose part of its scalar field and kinetic energy via energy transfer to internal oscillations of each star, gravitational cooling and gravitational wave radiation.

Motivated by the resemblance between the scalar field distribution of the final fate of a Q-star head-on binary and the scalar field distribution of a doublet Q-star we presented the dynamical evolution of eight different solutions, with four of them showing signs of an unstable behaviour. Three of those proved to migrate to a different solution, whose final state still requires further investigation. The

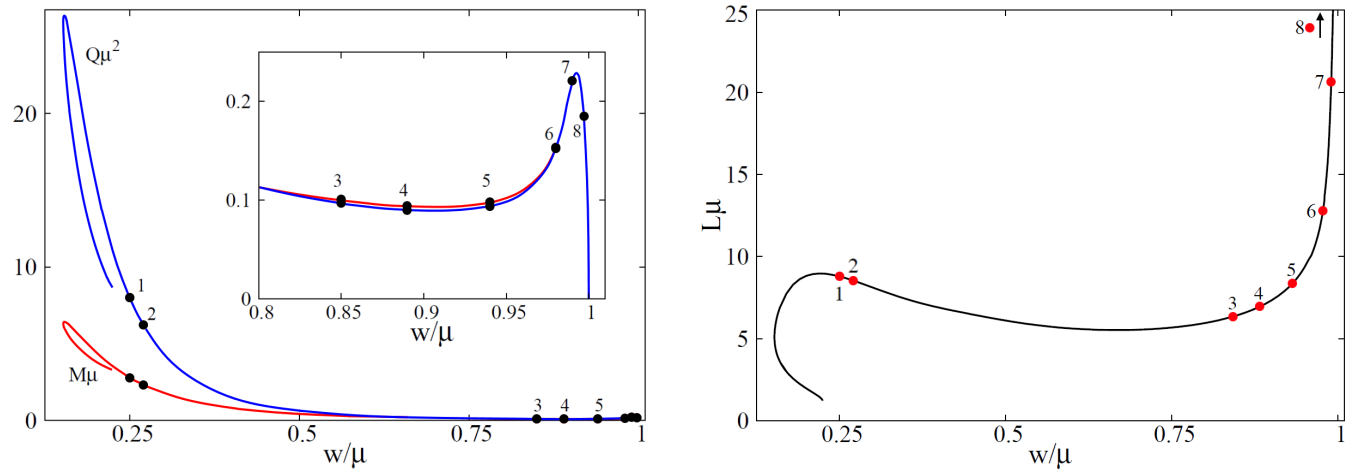

Figure 9: *Doublet Q-stars.* (Left) The domain of existence of doublet Q-stars in an ADM mass (M)/Noether charge (Q) *vs.* complex scalar field frequency (ω/μ) diagram. The inset shows the behaviour for the region close to the maximal frequency. (Right) The proper distance (L) between the two components, or poles, of each star as a function of the scalar field frequency (ω/μ). The eight highlighted points represent the solutions analysed in this Chapter.

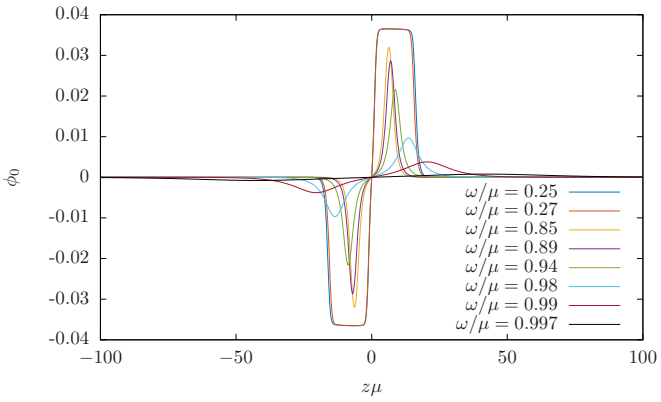

Figure 10: *Doublet Q-stars.* Real part of the scalar field along the $z-$ axis, at $t = 0$, for the eight solutions.

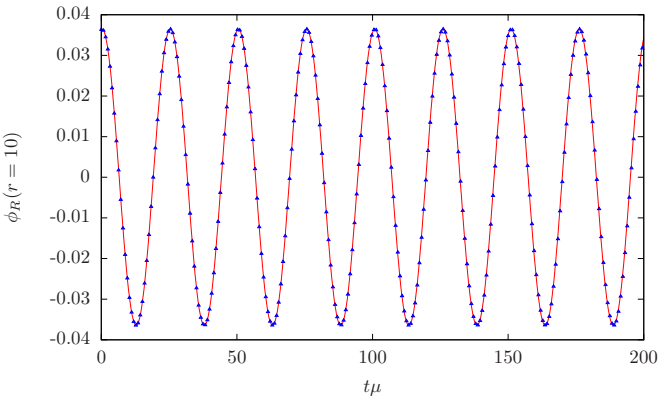

Figure 11: *Doublet Q-star with* $\omega/\mu = 0.25$. Evolution of the real part of ϕ at $r\mu = r_{\rm ex} = 10$. The analytical expected value — $0.036\cos(0.25\ t)$ — is illustrated as the red line while the numerical evolution is shown by the blue points.

hypothesis that the solutions with $\omega/\mu = \{0.94,\ 0.98\}$ migrate to the same stable branch as the $\omega/\mu = 0.99$ solution still requires the study of additional solutions in the frequency region of $\omega/\mu = [0.98\ 0.99]$. On the other hand, the fission of the solution with $\omega/\mu = 0.89$, due to an excess of binding energy, might indicate that the minimum in the $M_{\rm ADM}$ *vs.* ω/μ diagram in Figure 9 separates solutions with entirely different behaviours as the latter and the solution with $\omega/\mu = 0.94$. Additional solutions in the latter region are required to be studied in order to build a strong conclusion on the dynamical behaviour of doublet Q-stars.

Acknowledgements

All simulations were performed with the Minho Advanced Computer Center (MACC) and Infrastrutura Nacional de Computação Distribuída (INCD) Cirrus-B clusters at University of Minho, and the Baltasar clusters at IST.

References

[1] D. J. Kaup, *Phys. Rev.* **172**, 1331 (1968).

[2] J. C. Bustillo, *et al.*, *Phys. Rev. Lett.* **126**, 081101 (2021).

[3] C. A. Herdeiro, *et al.*, *Journal of Cosmology and Astroparticle Physics* **2021**, 051 (2021).

[4] V. Cardoso, P. Pani, *Living Reviews in Relativity* **22**, 4 (2019).

[5] R. Sharma, S. Karmakar, S. Mukherjee (2008).

[6] K. Danzmann, the LISA study team, *Classical and Quantum Gravity* **13**, A247 (1996).

[7] C. Herdeiro, J. Kunz, I. Perapechka, E. Radu, Y. Shnir, *Physics Letters B* **812**, 136027 (2021).

[8] M. Bezares, C. Palenzuela, C. Bona, *Phys. Rev. D* **95**, 124005 (2017).

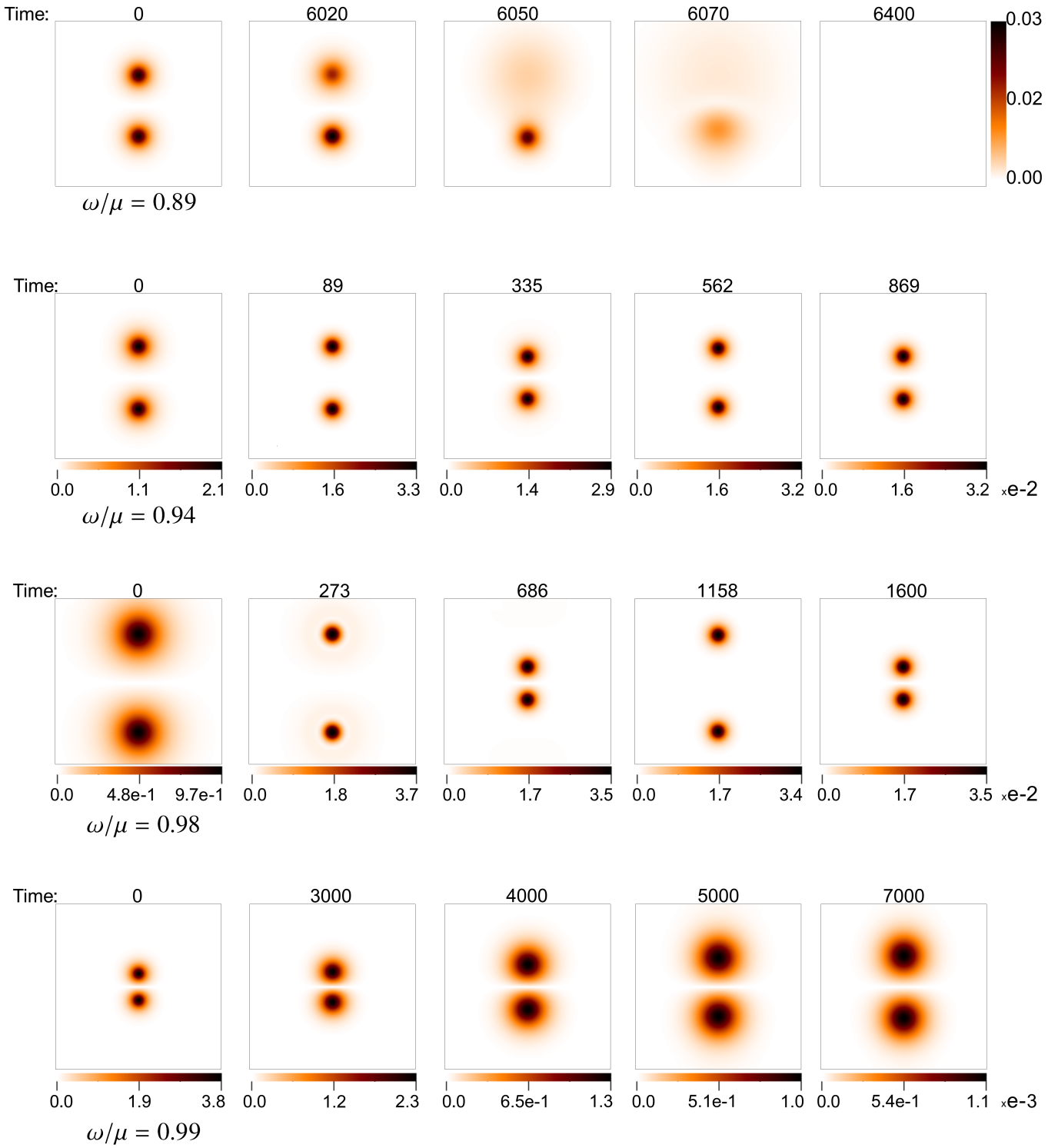

Figure 12: *Doublet Q-stars.* Time snapshots of the scalar field density in the plane $y = 0$ where each row, from top to bottom, corresponds to the 4th, 5th, 6th and 7th solutions. Except for the 4th solution, the colour table changes the scale for each snapshot to show the scalar field behaviour clearly. The snapshots presented here aim to show the most relevant phases that the unstable doublets go through. Link to movies [32].

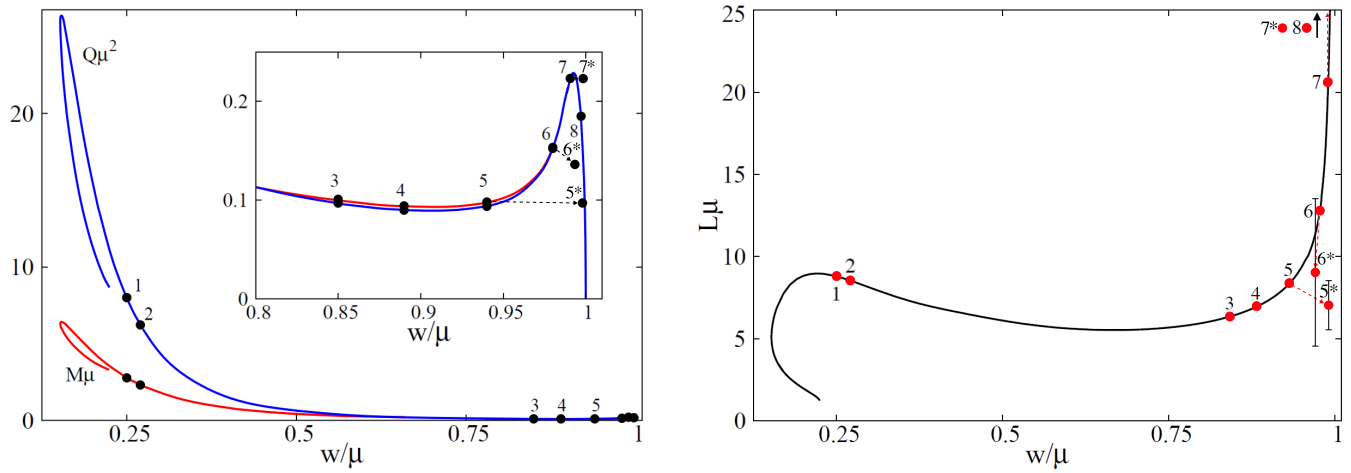

Figure 13: The domain of existence of doublet Q-stars with the preliminary migration directions of the 5th, 6th and 7th solutions, represented as 5*, 6* and 7*. (Left) The domain of existence of doublet Q-stars in an ADM mass (M)/Noether charge (Q) *vs.* complex scalar field frequency (ω/μ) diagram. The inset shows the behaviour for the region close to the maximal frequency. (Right) The proper distance (L) between the two components, or poles, of each star as a function of the scalar field frequency (ω/μ). The range of values for the solutions 5* and 6* illustrates the maximum and minimum distances reached by the poles due to their oscillating behaviour.

[9] E. Seidel, W.-M. Suen, *Phys. Rev. Lett.* **72**, 2516 (1994).

[10] M. Gleiser, R. Watkins, *Nuclear Physics B* **319**, 733 (1989).

[11] T. Lee, Y. Pang, *Nuclear Physics B* **315**, 477 (1989).

[12] C. Palenzuela, I. Olabarrieta, L. Lehner, S. L. Liebling, *Phys. Rev. D* **75**, 064005 (2007).

[13] C. Palenzuela, L. Lehner, S. L. Liebling, *Phys. Rev. D* **77**, 044036 (2008).

[14] I. Affleck, M. Dine, *Nuclear Physics B* **249**, 361 (1985).

[15] F. V. Kusmartsev, F. E. Schunck, *Physica B: Condensed Matter* **178**, 24 (1992). Proceedings of the Körber Symposium on Superfluid 3He in Rotation.

[16] F. V. Kusmartsev, E. W. Mielke, F. E. Schunck, *Phys. Rev. D* **43**, 3895 (1991).

[17] B. Thaller, *Visual quantum mechanics: selected topics with computer-generated animations of quantum-mechanical phenomena* (Springer Science & Business Media, 2007).

[18] P. Ildefonso, M. Zilhão, C. Herdeiro, E. Radu, *To appear* .

[19] M. Zilhão, F. Löffler, *International Journal of Modern Physics A* **28**, 1340014 (2013).

[20] Z. Etienne, *et al.*, The einstein toolkit (2021). To find out more, visit http://einsteintoolkit.org.

[21] T. W. Baumgarte, S. L. Shapiro, *Phys. Rev. D* **59**, 024007 (1998).

[22] M. Shibata, T. Nakamura, *Phys. Rev. D* **52**, 5428 (1995).

[23] M. Alcubierre, *et al.*, *Phys. Rev. D* **67**, 084023 (2003).

[24] Cactus computational toolkit (2021). URL http://www.cactuscode.org/.

[25] T. Goodale, *et al.*, *High Performance Computing for Computational Science — VECPAR 2002* (Springer Berlin Heidelberg, Berlin, Heidelberg, 2003), pp. 197–227.

[26] H. Witek, *et al.*, Canuda: a public numerical relativity library to probe fundamental physics (2021).

[27] C. Herdeiro, E. Radu **32**, 144001 (2015).

[28] P. Bowcock, D. Foster, P. Sutcliffe, *Journal of Physics A: Mathematical and Theoretical* **42**, 085403 (2009).

[29] P. V. P. Cunha, *et al.*, *Phys. Rev. D* **96**, 104040 (2017).

[30] Movie for q-star in-phase head-on collision (2021). Available online at: `https://youtu.be/eD_ZqtEoRC0`, last accessed on 10-October-2021.

[31] Movie for q-star in phase opposition head-on collision (2021). Available online at: `https://youtu.be/DbC7i31lLiE`, last accessed on 10-October-2021.

[32] Movie for the dynamical evolution of doublet q-stars (2021). Available online at: `https://youtube.com/playlist?list=PLlUPX3-jdZEltlLqy5wVA9Z7RU83MIKUv`, last accessed on 10-October-2021.